

# Discovery of Promising Inhibitors for SARS-CoV-2 Therapeutic Targets: A Quantum Mechanics and Molecular Modeling study

**Toheeb A. Balogun** (✉ [baloguntoheeb685@gmail.com](mailto:baloguntoheeb685@gmail.com))

University of California, San Diego

**Onyeka S. Chukwudozie**

University of California, San Diego

**Uchechuckwu C. Ogbodo**

Nnamdi Azikiwe University

**Idris O. Junaid**

Stevens Institute of Technology

**Olugbodi A. Sunday**

Universitat Duisburg-Essen

**Oluwasegun M. Ige**

Ghent University

**Abdullahi T. Aborode**

Mississippi State University

**Abiola D. Akintayo**

The University of Texas at Dallas

**Emmanuel A. Oluwarotimi**

Missouri University of Science and Technology

**Isaac O. Oluwafemi**

Adekunle Ajasin University Akungba-Akoko

**Tosin A. Saibu**

Universitat Duisburg-Essen

**Prosper Chuckwuemaka**

Federal University of Technology Akure

**Damilola A. Omoboyowa**

Adekunle Ajasin University Akungba-Akoko

**Gaber E. Batiha**

Damanhour University

---

## Research Article

**Keywords:** SARS-CoV-2, COVID-19, 3CLpro, PLpro, RdRp, Molecular Modeling, Glycoprotein

**Posted Date:** April 1st, 2022

**DOI:** <https://doi.org/10.21203/rs.3.rs-1403394/v1>

**License:** © ⓘ This work is licensed under a Creative Commons Attribution 4.0 International License. [Read Full License](#)

---

# Abstract

SARS-CoV-2 triggers a worldwide medical crisis, affecting the world's social, emotional, physical, and economic equilibrium. However, treatment choices and targets for finding a solution to COVID-19's threat are becoming limiting. A viable approach to combating the threat of COVID-19 is to create pharmacological and therapeutic targets by uncovering promising inhibitors and proteins in the viral life cycle of COVID-19. Therefore, in this study, we employ high-throughput virtual screening to screen library of phytochemicals from selected medicinal plants targeting SARS-CoV-2 spike glycoprotein, 3CLpro, PLpro and RdRp. Virtual screening approach have been reported as a promising method to identify biologically active compounds from large libraries. In addition, molecular docking, Prime MM/GBSA (molecular mechanics/generalized born surface area) analysis, molecular dynamics (MD) simulation and pharmacokinetic/drug-likeness model was performed to identify potential phytodrugs. In support to these approaches, we employ series of chemical quantum calculation, semi empirical Hamiltonian and density functional theory analysis to develop therapeutic agents against COVID-19. We propose that the discover therapeutic targets/molecules may open the way for the establishment of phytodrugs for the management of COVID-19 pandemics and new chemical libraries for preventing COVID-19 entry into the host, based on the findings of this integrated computational investigation.

## 1.0 Introduction

With the emergent of different variations of the corona virus disease 2019 (COVID-19) such as alpha, delta and Omicron, COVID-19 remained a global challenge to health and the economy due to the unexpected emergence of severe acute respiratory syndrome coronavirus-2 (SARS-CoV-2). COVID-19 is an agile respiratory disease caused by novel coronavirus which was first reported in Wuhan, China in December 2019 and declared a global pandemic by the World Health Organization (WHO) in March 2020 (1). Coronaviruses are positive sensed, linear single stranded-stranded RNA viruses which comprises of nucleoproteins (N), envelope proteins (E), matrix proteins (M), spike proteins (S), and many non-structural proteins (2). The length of the RNA genomes ranges from 26–32 kilobase which contains 12 open reading frames. Structural analysis of the SARS-CoV-2 genomes using biophysical and modeling techniques reveals that two polyproteins which are divided into 15 or 16 non-structural proteins makeup the first two-thirds of the coronavirus genome (3). Phylogenetic analysis shows that the remaining ORFs contains the genetic makeup of four important structural proteins: envelop (E), membrane (M), nucleocapsid (N) and spike (S) proteins. These proteins play significant role in the virus survival, replication and had have received intense interest by several investigators to develop inhibitors of SARS-CoV-2 (4–6). Notably, COVID-19 has been associated with effect on multiple vital organ, central nervous system and can result in respiratory problems with fatal consequences (7). Previous reports indicated that SAR-CoV-2 therapeutic targets include receptor binding of glycosylated spike (S) protein, which mediates host cell receptor recognition and host cell entry, and induces host immune responses; and (ii) non-structural proteins such as RNA-dependent RNA polymerase (RdRp), the CoV main protease (Mpro; also known as 3-chymotryp-sin-like protease (3CLpro)) and papain-like protease (PLpro) (8). Theoretically, drugs that compete with RBD for receptor binding sites can inhibit viral entry and its replication. Furthermore, the non-structural proteins (PLpro, 3CLpro, and RdRp) play a vital role in proteolysis and viral polyprotein processing. Thus, NSPs had recently emerged as important therapeutic biomarker for the design of COVID-19 drug candidates (9).

The therapeutic management of COVID-19 involves two target selection approach. One of the method is boosting the human immune system or human cells using attenuated vaccine while the second techniques involves inhibiting molecular targets by small molecule inhibitors. Regarding the human immune system, the innate immune system plays a key role in the disruption of the coronavirus replication and its entry. As expected, the interferon helps to enhance immune response towards the virus (10). One of the most effective way to halt the viral replication and entry is the use of small molecules to block the signaling pathways of the cells human which mediate the virus replication. Furthermore, viruses interact with certain receptor proteins on the surface of cells to gain entry into human cells. Notably, RBD of SARS-CoV-2 binds with the human angiotensin converting enzyme 2 (ACE2) receptor (11–13).

Several strategies have been harnessed by scientist towards the development of novel drugs against COVID-19 (14). The first strategy is to screen existing broad-spectrum anti-viral drugs such as ribavirin and cyclophilin. This approach is advantageous because of known pharmacokinetics profile of the antiviral drugs and their associated side effect have been clearly stated. One of the disadvantages of broad-spectrum antiviral drugs is their non-specificity which might in turn results in low-potency against coronavirus (15,16). The second techniques involve the screening of molecular databases such as ZINC database to identify potential anti-coronavirus compounds via high-throughput virtual screening. This approach has been employed to developed biologically active compounds; lopinavir/ritonavir as anti-HIV agents (16). The third approach is based on analysis of genomic dataset to develop new targeted drug candidates from scratch towards precision medicine (17). Therapeutic agents developed against coronavirus via the third strategy will exhibit promising pharmacological potential. However, the long-term process and expenses associated with this approach is a major limiting factor (18).

Herbal medicine has been used as an alternative medicine since time immemorial in the management of various diseases and may be an important source of anti-coronavirus agent (19). Earlier systematic study in 2003 shows that patients infected with SARS-CoV-2 treated with traditional Chinese medicine (TCM) were reported to short time hospitalization, reduced steroid side effects and improvements from the viral symptoms (20). Therefore, a significant amount of research study has focused on the development of therapeutic agent against coronavirus from TCM, ethnobotanical herbs and dietary supplements (21,22). In vivo, invitro and insilico studies have revealed the anti-viral potential of

numerous bioactive compounds against coronavirus. Some the phytochemicals and source include: glycyrrhizin isolated from *Glycyrrhiza glabra* L. (licorice), tetra-O-galloyl- $\beta$ -D-glucose (TGG) and luteolin, isolated

from *Rhus chinensis* Mill. and *Veronica linariifolia* Pall. ex Link, aurantiamide acetate derived from *Artemisia annua* L. plant and many others. Several plants such as *Sanguisorba officinalis* L., *Stephania tetrandra* S. Moore, and *Strobilanthes cusia* (Nees) Kuntze have been reported for their anti-viral potential towards RNA and protein synthesis of the coronavirus (23–25). Therefore, in this study, we employed high-throughput virtual screening to screen library of phytochemicals from selected medicinal plants targeting SARS-CoV-2 spike glycoprotein, 3CLpro, PLpro and RdRp. Virtual screening approach have been reported as a promising method to identify biologically active compounds from large libraries. Furthermore, molecular docking, Prime MM/GBSA (molecular mechanics/generalized born surface area) analysis, molecular dynamics (MD) simulation and pharmacokinetic/drug-likeness model was performed to identify potential phytochemicals. In addition to this approaches, we employed series of chemical quantum calculation, semi empirical Hamiltonian and density functional theory analysis to develop therapeutic agents against COVID-19. We believed that results from this integrated computational study would pave a way to development phytochemicals for the management of COVID-19 pandemic.

## 2.0 Materials And Method

### 2.1 Quantum mechanical calculation

Theoretical approaches employed to compute the chemical and biological activities of compounds have been well documented. The quantum chemical (QM) calculation was executed using the MOPAC 2016 software program (26). PM7 semi-empirical Hamiltonian incorporating an implicit COSMO solvation model was employed to perform the calculation (27,28). Notably, geometric pre-optimization of the top four inhibitors were carried out using the molecular mechanics force field (MMFF94) integrated in Avogadro v1.2.0 software program (29), coupled chemical structure protonation at a pH of 7.4. The pre-optimized geometry serves as query for QM calculation (30). Broyden-Fletcher-Goldfarb-Shanno (BFGS) geometry optimizer was employed for structure minimization and optimization at semi-empirical theory level. The keywords "DIPOLE" and "MULLIK" were used to compute the dipole moments and Mulliken atomic charges respectively. The Time-Dependent Hartree Fock (TDHF) was used to calculate the molecular polarizabilities using the "POLAR" keyword as incorporated in MOPAC 2016. A visualization tool (Jmol software program) was used to visualize the charge distribution diagram of frontier molecular orbitals (FMOs) and molecular electrostatic potential (MEP) of the docked compounds (31). A quantum chemical calculation via density functional theory (DFT) was employed to investigate the physicochemical properties of lead phytochemicals with the best conformer distribution. All the quantum chemical reactivity descriptors were computed from the energies of highest occupied and lowest unoccupied molecular orbitals ( $E_{\text{HOMO-LUMO}}$ ). The descriptors include: energy band gaps ( $E_g$ ), ionization energy ( $I$ ), electron affinity ( $A$ ), chemical hardness ( $\eta$ ), chemical softness ( $\delta$ ), chemical potential ( $\mu$ ), electronegativity ( $\chi$ ).

### 2.2 Molecular docking studies

#### 2.2.1 Protein and ligand preparation

The crystal structures of the molecular targets RBD of spike glycoprotein (PDB: 6MOJ), 3CLPro (PDB: 6M2N), PLPro (7CJM) and RDRP (7D4F) were obtained from the protein data bank (<https://www.rcsb.org/>), and were prepared using the Schrödinger's protein preparation wizard (32). Hydrogen bond optimizations, water removal, protein structure correction, and ultimately protein energy minimization using OPLS\_2005 force field were carried out during the

preparation. The position of the co-crystallized ligands for each target was used to define the protein binding pocket for receptor grid generation. Subsequently, the 3D structure of 1000 compounds consisting of substructure of the co-crystallised ligand of the targets were downloaded from PubChem database (<https://pubchem.ncbi.nlm.nih.gov>). The structures of the ligands were cleaned and their geometries were subjected to structural optimization using the default specifications of the LigPrep module and utilized for hypothesis generation (33). The prepared proteins and fully optimized geometry of ligands were used as input for molecular docking.

#### 2.2.2 Molecular docking

High-throughput virtual screening (HTVS) of the prepared phytochemicals library was performed using the HTVS module of Maestro integrated in Schrodinger suite (34). The HTVS module employed the 3D crystallographic structure of the therapeutic targets and fitted the ligands based on their structural conformations. During the virtual screening process, an energy score of -5.0kcal/mol was set as threshold to identify potential anti-coronavirus agents. The hits generated which was 105 compounds out of 1000 screened phytochemicals where subjected to molecular docking by considering the flexibility of the protein using the SP (standard precision) model. To further achieve accurate results based on binding affinity and binding poses, the compounds where subjected to XP (extra precision) docking using the GLIDE XP module incorporated in Maestro. The structural and energy information between the protein-ligand complex was considered for energetic computation and further stability studies. The 2D interaction profile of protein-ligand complexes were generated using Ligand Interaction Diagram (LID) in Maestro (34, 35). The

reproducibility and reliability of the docking procedure was validated by superimposing and re-docking the co-crystallized ligand structures into the target active site which generated an RMSD value of 0.76 Å (Normal range 0–2 Å). This confirms the reliability of the docking protocol.

## 2.3 Molecular Dynamics Simulation

Molecular dynamics (MD) simulations were conducted to predict the protein's dynamic motion and stability at the atomistic level with the bounded protein. DESMOND module integrated in Schrodinger suite was employed to generate protein-ligand topologies and trajectories. The protein-ligand complexes were performed for 100 ns with OPLS3 force field, using DESMOND version of Schrodinger (35). The solvation box was designed as the shape of the rhombic dodecahedron type and solvated using the TIP3P (transferable intermolecular potential-4-point), and an orthorhombic box (10 X 10 X 10 Å buffer) water model. Na<sup>+</sup> and Cl<sup>-</sup> ions in 0.15 M concentration were added to neutralize the charge of the systems during simulation. The system minimization tool in the Desmond-Maestro interface was employed for energy minimization of the complete system under default parameters of 1.0 kcal/mol/Å, convergence threshold, and maximum iterations of 2000. Furthermore, the system was calibrated with the constant temperature (300 K) and pressure (1 bar) via Berendsen thermostat coupling and default system pressure coupling, respectively. Each of the equilibration steps

was carried out for 100 ps. The dynamic simulation of the complex system was performed for 10 ns after all the pre-processing phases. The V-rescale and Parrinello-Rahman methods were employed for temperature and pressure coupling respectively (36). Leonard-Jones potentials and Particle Mesh Ewald (PME) method were used to handle van der Waals and long-range electrostatic interactions respectively (37). The complexes were subjected to a final MD simulation production run for 100 ns. Root-mean square deviations (RMSD) were computed using the MD trajectory to estimate the variations in protein conformation during the various simulation periods and Root mean square fluctuation (RMSF) as well as the total number of intermolecular contacts for each protein–ligand complex to gain insights into the compound's inhibitory potential (38).

## 2.4 Binding free energy and contribution energies calculation using MM-PBSA

The XP screened compounds were further subjected to Prime MM/GBSA analysis where their binding energies were computed to investigate the inhibitory potential of the docked compounds against the targets. Based on the number of energy parameters generated by the Prime algorithm, free energy parameters were employed to gain mechanistic insight into the biological activity of the compounds. Nonetheless, the ligand strain energy, Coulomb energy, and Van der Waals energy were also assessed in filtering of the final hit compounds (39,40). The binding free energy and essential amino acid interaction between the protein-ligand complex was computed using the equation below:

$$\Delta G_{\text{bind}} = \Delta E + \Delta G_{\text{solv}} + \Delta G_{\text{SA}} \quad (1)$$

$$\Delta E = E_{\text{complex}} - E_{\text{protein}} - E_{\text{ligand}} \quad (2)$$

Where,  $E_{\text{complex}}$ ,  $E_{\text{protein}}$  and  $E_{\text{ligand}}$  are the minimized energies of the protein–inhibitor complex, protein, and inhibitor, respectively.

$$\Delta G_{\text{solv}} = G_{\text{solv}}(\text{complex}) - G_{\text{solv}}(\text{protein}) - G_{\text{solv}}(\text{ligand}) \quad (3)$$

Where,  $G_{\text{solv}}(\text{complex})$ ,  $G_{\text{solv}}(\text{protein})$ , and  $G_{\text{solv}}(\text{ligand})$  are the solvation free energies of the complex, protein, and inhibitor, respectively.

$$\Delta G_{\text{SA}} = G_{\text{SA}}(\text{complex}) - G_{\text{SA}}(\text{protein}) - G_{\text{SA}}(\text{ligand}) \quad (4)$$

Where  $G_{\text{SA}}(\text{complex})$ ,  $G_{\text{SA}}(\text{protein})$ , and  $G_{\text{SA}}(\text{ligand})$  are the surface area energies for the complex, protein, and inhibitor, respectively.

## 2.5 Drug-likeness, and ADMET evaluation

To compute their physico-chemical parameters and pharmacokinetic models, the inputted structures were transformed to their canonical simplified molecular-input line-entry system (SMILE). Therefore, the curated ligand database's SMILES were uploaded to the admetSAR web server (<http://lmmd.ecust.edu.cn/>) (41) and SWISS ADME (42). Drug-likeness is a method for determining if a therapeutic agent is appropriate for orally active medications. Lipinski's rule of five principles is used to compute in silico predictions based on parameters such as molecular weight, hydrogen bond donor, and acceptor (43).

## 3.0 Results And Discussion

### 3.1 Frontier molecular orbital analysis (FMO) and global reactivity descriptors

FMO such as HOMO and LUMO plays an important role in demystifying the chemical reactivity at the atomistic level and are crucial descriptors for the rationalization of various chemical reactions. The reactivity descriptors calculated for Ionchocarpol A, Broussonol A, Diplacol and Dexamthasone are shown in Table 1. HOMO energy denotes the potential of a molecule to easily donate an electron which also corresponds to

the ionization potential of a molecule. In contrast, the electron withdrawing potential of a compounds is referred to as the LUMO energy which signifies the first empty innermost orbital unfilled by electron and also correlate with the electron affinity of a molecule. The band gap energy is the difference between the HOMO and the LUMO energy and provide information about the compound's chemical stability at the molecular level. Band gap energy also describes chemical reactivity of a molecule deciphering movement of electron from the ground state to its excitation state. Furthermore, Other parameters (such as chemical hardness, softness, electronegativity or polarizability) that provides information about compounds ionic structure and the electronic configuration can be easily computed via the HOMO-LUMO energy (44,45). For example, a lower energy gap between two frontier molecular orbitals means a lower kinetic stability, higher polarizabilities and reactivity of a molecule which indicates the softness of the molecule and vise-versa.

Table 1  
Calculated quantum reactivity descriptors of top four compounds using PM7 Hamiltonian method.

SN	Quantum chemical property	Lonchocarpol A	Broussonol E	Diplacol	Dexamethsaone
1	HOMO	-8.776 eV	-8.647 eV	-8.763 eV	-9.964 eV
2	LUMO	-0.501 eV	-1.117 eV	-0.902 eV	-0.501 eV
3	Energy Gap ( $\Delta E$ )	-8.275 eV	-7.530 eV	-7.861 eV	-8.275 eV
4	Ionization potential (I)	8.776 eV	8.647 eV	8.763 eV	8.776 eV
5	Electron affinity (A)	0.501 eV	1.117 eV	0.902 eV	0.501 eV
6	Chemical hardness ( $\eta$ )	4.138 eV	3.765 eV	3.931 eV	4.138 eV
7	Chemical softness ( $\zeta$ )	0.242 (eV) <sup>-1</sup>	0.267 (eV) <sup>-1</sup>	0.254 (eV) <sup>-1</sup>	0.242 (eV) <sup>-1</sup>
8	Electronegativity ( $\chi$ )	4.639 eV	4.882 eV	4.833 eV	4.639 eV
9	Chemical potential ( $\mu$ )	-4.634 eV	-4.882 eV	-4.833 eV	-4.634 eV
10	Electrophilicity index ( $\omega$ )	2.595 eV	3.165 eV	2.971 eV	2.595 eV
$\Delta E = \text{HOMO}\epsilon - \text{LUMO}\epsilon, I = -E_{\text{HOMO}}, A = -E_{\text{LUMO}}, \eta = (I - A)/2, \zeta = 1/\eta, \chi = (I + A)/2,$					

$$\mu = -(I + A)/2, \omega = \mu^2/2\eta$$

Lonchocarpol A has the second highest HOMO orbital energy value ( $E_{\text{HOMO}} = -8.77\text{eV}$ ) denoting that the valence valence electron density distribution for Lochocarpol A is more available to be donated, therefore, suggesting Lonchocarpol A as the most reactive compound after dexamethasone. Similarly, Broussonol E and Diplacol recorded a HOMO energy value of -8.647 eV and - 8.763 eV respectively. Clearly, Lonchocarpol A, Broussonol E and Diplacol demonstrated an intermolecular charge transfers as they excited from the ground state ( $S_0$ ) to the first excitation state (Fig. 1). Interesting, the LUMO energy are in the order: Lochocarpol A < Dexamethasone < Diplacol < Broussonol E. The LUMO energy suggests that Lonchocarpol A and Dexamethasone are more susceptible to accept electronic density since the additional electron will be described by lower energy molecular orbital. The chemical reactivity of a compound is measured using the HOMO-LUMO energy gap ( $\Delta E_{\text{Gap}}$ ) which represent lower energy difference (lower energy gap) (Fig. 1).

Broussonol E had the lowest energy value of -7.530 eV when compared to Dexamethasone (-8.275 eV) which implies more chemical reactivity to Broussonol E. Interestingly, Lonchocarpol A and Dexamethasone showed the same energy gap (-8.275 eV) which is in consistent with their LUMO values. This suggest that both the compounds may share similar chemical reactivity properties and mechanism of action toward the targets. To fully gain insights into the reactivity and chemical species of the top four compounds with drug-likeness properties, the following parameters were evaluated from the HOMO and LUMO energy: ionization potential, electron affinity, chemical hardness ( $\eta$ ), chemical softness ( $\zeta$ ), electronic chemical potential ( $\mu$ ), Electrophilicity index ( $\omega$ ), and electronegativity ( $\chi$ ). The expression for the aforementioned reactivity parameters has been described according to Koopman's theore (46), and can be calculated by the accompanying mathematical statements;

$$\text{Energy Gap } \Delta E = \text{HOMO}_e - \text{LUMO}_e \quad (3)$$

$$\text{Ionization Potential } I = -E_{\text{HOMO}} \quad (4)$$

$$\text{Electron affinity } A = -E_{\text{LUMO}} \quad (5)$$

$$\text{Chemical hardness } \eta = \frac{1}{2} \left( \frac{\partial^2 E}{\partial N^2} \right) V = \frac{1}{2} \left( \frac{\partial \mu}{\partial N} \right) V = (I - A) / 2 \quad (6)$$

$$\text{Chemical potential } \mu = \left( \frac{\partial E}{\partial N} \right) V = -(I + A) / 2 \quad (7)$$

$$\text{Electronegativity } \chi = -\mu = - \left( \frac{\partial E}{\partial N} \right) V = (I + A) / 2 \quad (8)$$

$$\text{Softness } \zeta = \frac{1}{\eta} \quad (9)$$

$$\text{Electrophilicity index } \omega = \frac{\mu^2}{2\eta} \quad (10)$$

Ionization energy helps to determine the amount of free energy required to remove an electron of an atom from a molecule. Furthermore, Electron affinity represent the amount of energy liberated when an atom or molecule is attached to a neutral atom or molecule. Lower ionization potential indicates a lower stability or higher reactivity of the compound and its contribution towards analyzing inhibitory potential. Contrarily, electron affinity depicts the high-electron withdrawing ability of a compound. Table 1 shows that Lonchocarpol A and Dexamethasone had the highest chemical stability and electron withdrawing potential when compared to Broussonol E and Diplacol. This observation is consistent with the gap energy between the HOMO and LUMO FMOs (Fig. 2). Softness and hardness properties of a compound contribute towards its chemical stability. While a higher hardness value means a more stable chemical entity, a compound's stability decreases with softness. Pearson's HSAB theory proposed that a favorable interaction between two compounds occurs when both are hard and soft (47,48). It is evident from Table 1 that Lonchocarpol A and Dexamethasone have the highest chemical hardness values; 4.138 eV indicating they are the most stable compound followed by Diplacol (3.931 eV) and Broussonol E (3.765). The chemical softness of the compounds shows that there is only a subtle difference between the compounds denoting their chemical stability. The ability of a compound to not decompose spontaneously into an element which denotes its stability is determined by a higher negative chemical potential. All the compounds demonstrated chemical stability due to their negative value of chemical potential. Electronegativity and electrophilicity are another important set of reactivity descriptors. Lonchocarpol A and Dexamethasone have the same electrophilicity index (2.595 eV) and electronegativity values (4.639 eV) which implies their susceptibility to accept electron density and classify them as promising electrophilic compounds. Broussonol E was recorded as the most electrophilic molecule with an electrophilicity index value of 3.165 eV. Therefore, Table 1 provides appropriate information regarding the chemical reactivity and stability of the studied compounds.

### 3.2 Molecular electrostatic potential (MEP)

MEPs have proved useful in determining the relative polarity of compounds as well as providing essential information on molecular charge distribution patterns. As a result, studying the MEP of the examined compounds may provide insight into their electrophilic and nucleophilic cores. It's worth mentioning that molecular electrostatic potential data can be classified using traditional color codes. The electron-rich centers are indicated by a red color scheme, which symbolizes the highest negative electrostatic potential. A blue hue region, on the other hand, denotes electron-deficient areas (i.e. the most positive electrostatic potential). The light blue, yellow, and green color moieties, respectively, represent a molecule's region of slightly electron-deficient cores, marginally electron-rich areas, and zero electrostatic potential portions (Fig. 2). We can deduce that a molecule's potential declines in the following order based on the color scheme: blue > light blue > green > yellow > red. Figure 2, represent molecular electrostatic potential maps of Lonchocarpol A, Broussonol E, Diplacol and Dexamethasone. It is very clear there is maximum concentration of electrons located at the alkyl groups and oxygen atoms of Lonchocarpol A attached to the diphenyl groups.

In contrast, the region of most positive electron potential of Lonchocarpol A is located at the hydrogen atoms of methyl group of the phenyl group. The most negative potential for Dexamethasone is located on the two-hydroxyl group and oxygen atoms of the imidazole rings. Broussonol E recorded the highest negative electrostatic potential including multiple hydroxyl groups points. All the compounds have been reported for their biological and chemical properties. Therefore, MEP provides detailed insights into the molecular charge distribution clusters in the studied compound.

### 3.3 Mulliken population analysis

Table 2 shows the atomic charge distribution of Lonchocarpol A, Broussonol E, Diplacol and Dexamethasone computed via the Mulliken population analysis using the PM7 based semi-empirical Hamiltonian calculations. Because atomic charges affect the molecular and electrical characteristics of compounds, estimating partial atomic charges of each compound is critical for understanding the charge distribution. Calculating the atomic charges of any small molecule ligand can be used to calculate the adsorptive centers. Table 2 shows that the examined structures' oxygen and carbon atoms have electron-rich chemical species (i.e., they have the most negative electronic charges), which may be due to their molecular relaxation. However, the predominant positive charge regions were observed to be covered by carbon atoms. Despite the fact that some carbon atoms in the investigated compounds possessed negative atomic charges. Table 2 shows that the atoms O7, C9, and C27-30 of Lonchocarpol have the most negative atomic charges, whereas the C11 and C16 of Broussonol E have the highest negative atomic charges in Lonchocarpol A. In terms of Broussonol E; C10, C16 were observed for negatively charged atoms while C11 and C15 occupied positive regions.

Dexamethasone ionic structure established negative charges electrostatic contacts with C18 and C22-23 while demonstrating C27 as the only positive electrostatic atoms. Overall, it can be deduced that, there are variations between the atoms of the studied compounds occupying positive and negative regions. This is also supported by the difference between the compound inhibitory potentials and their chemical stability.

Table 2  
Calculated Mulliken atomic charges of the top four compounds.

Atom No	Atom (Lonchocarpol A)	Mulliken charge (Lonchocarpol A)	Atom (Broussonol E)	Mulliken charge (Broussonol E)	Atom (Diplacol)	Mulliken charge (Diplacol)	Atom (Dexamethasone)	Mulliken charge (Dexamethasone)
1	O	-0.44443	O	-0.34135	O	-0.43335	F	-0.22161
2	O	-0.52506	O	-0.5126	O	-0.57712	O	-0.57211
3	O	-0.49887	O	-0.48847	O	-0.5101	O	-0.59853
4	O	-0.59159	O	-0.45938	O	-0.57763	O	-0.47831
5	O	-0.51036	O	-0.59099	O	-0.49375	O	-0.5496
6	C	0.207278	O	-0.53436	O	-0.47351	O	-0.50928
7	C	<b>-0.64918<sup>a</sup></b>	O	-0.48846	O	-0.47101	C	0.119523
8	C	0.553263	C	<b>-0.68688<sup>a</sup></b>	C	0.111928	C	-0.17951
9	C	<b>-0.73661<sup>a</sup></b>	C	-0.45146	C	-0.09313	C	-0.19425
10	C	-0.37697	C	0.553329	C	<b>-0.73622<sup>a</sup></b>	C	0.167313
11	C	<b>0.702303<sup>b</sup></b>	C	<b>0.602767<sup>b</sup></b>	C	<b>0.601256<sup>b</sup></b>	C	0.126795
12	C	-0.45972	C	0.219836	C	0.597236	C	-0.40441
13	C	0.597616	C	0.012863	C	-0.03862	C	-0.51737
14	C	0.506552	C	-0.21543	C	-0.4738	C	-0.07233
15	C	-0.20439	C	0.532411	C	<b>0.611783<sup>b</sup></b>	C	0.110405
16	C	-0.21769	C	<b>0.620079<sup>b</sup></b>	C	<b>-0.6357<sup>a</sup></b>	C	-0.00231
17	C	-0.2394	C	-0.02945	C	-0.23452	C	-0.32459
18	C	-0.06819	C	<b>-0.60901<sup>a</sup></b>	C	0.561417	C	<b>-0.62434<sup>a</sup></b>
19	C	-0.01567	C	-0.06649	C	-0.33019	C	-0.41779
20	C	-0.32883	C	-0.22206	C	-0.14207	C	0.177623
21	C	-0.35013	C	-0.3368	C	-0.36668	C	0.407181
22	C	-0.35526	C	-0.25838	C	0.123515	C	<b>-0.60478<sup>a</sup></b>
23	C	-0.44732	C	0.104187	C	-0.39687	C	<b>-0.60459<sup>a</sup></b>
24	C	0.158178	C	0.234676	C	0.215686	C	-0.11383
25	C	0.371538	C	-0.37461	C	-0.34313	C	-0.52143
26	C	0.137273	C	-0.34269	C	-0.29078	C	-0.23229
27	C	<b>-0.64618<sup>a</sup></b>	C	0.210516	C	0.227416	C	-0.43236
28	C	<b>-0.65128<sup>a</sup></b>	C	0.149934	C	-0.65057	C	<b>0.621716<sup>b</sup></b>
29	C	<b>-0.64474<sup>a</sup></b>	C	-0.66075	C	-0.33623	H	0.174307
30	C	<b>-0.65366<sup>a</sup></b>	C	-0.66589	C	0.161681	H	0.199263

<sup>a</sup> Most negatively charge region.

<sup>b</sup> Most positively charge region.

Atom No	Atom (Lonchocarpol A)	Mulliken charge (Lonchocarpol A)	Atom (Broussonol E)	Mulliken charge (Broussonol E)	Atom (Diplacol)	Mulliken charge (Diplacol)	Atom (Dexamethasone)	Mulliken charge (Dexamethasone)
31	H	0.177918	C	-0.64924	C	-0.65057	H	0.18274
32	H	0.260334	C	-0.65697	C	-0.64239	H	0.202663
33	H	0.257829	H	0.202691	H	0.209879	H	0.217255
34	H	0.180081	H	0.147876	H	0.229331	H	0.223055
35	H	0.186761	H	0.290018	H	0.291301	H	0.155531
36	H	0.170022	H	0.224598	H	0.172566	H	0.197823
37	H	0.214067	H	0.192595	H	0.212728	H	0.181412
38	H	0.193514	H	0.204748	H	0.248627	H	0.185519
39	H	0.206486	H	0.264391	H	0.222298	H	0.21967
40	H	0.201087	H	0.195052	H	0.216964	H	0.193173
41	H	0.217387	H	0.21727	H	0.371795	H	0.211806
42	H	0.413892	H	0.41358	H	0.196626	H	0.200817
43	H	0.376606	H	0.367127	H	0.185069	H	0.208468
44	H	0.242263	H	0.37573	H	0.218915	H	0.191525
45	H	0.226644	H	0.214546	H	0.170655	H	0.211997
46	H	0.204763	H	0.210442	H	0.176395	H	0.217508
47	H	0.204729	H	0.206894	H	0.41009	H	0.209823
48	H	0.202827	H	0.205874	H	0.220548	H	0.221053
49	H	0.229196	H	0.236009	H	0.200566	H	0.211325
50	H	0.203416	H	0.209537	H	0.214513	H	0.362716
51	H	0.199179	H	0.378383	H	0.382286	H	0.222359
52	H	0.207816	H	0.210921	H	0.194678	H	0.354091
53	H	0.210879	H	0.213816	H	0.349727	H	0.252387
54	H	0.209347	H	0.21176	H	0.347314	H	0.231837
55	H	0.208034	H	0.206996	H	0.207703	H	0.204019
56	H	0.20602	H	0.219071	H	0.210102	H	0.244501
57	H	0.216366	H	0.211674	H	0.204851	H	0.356402
58	H	0.354056	H	0.36951	H	0.207125	-	-
59	-	-	-	-	H	0.205716	-	-
60	-	-	-	-	H	0.207643	-	-
<sup>a</sup> Most negatively charge region.								
<sup>b</sup> Most positively charge region.								

### 3.4 Nonlinear optics (NLO) analysis

NLO materials have played an important role in contemporary technologies, providing a variety of industrial and medicinal benefits, some of which have been detailed in prior studies (49, 50). The most prominent qualities of analyzing NLO properties, from a more fascinating perspective on chemical methodologies and applications, is their tendency to provide considerable insights into how small changes in molecular structures might alter NLO responses. Tables 3 and 4 present and summarize the various NLO responses and their components for Lonchocarpol

A, Broussonol E, Diplacol and Dexamethasone estimated using the PM7 semi-empirical Hamiltonian calculations in MOPAC 2016. The dipole moment ( $\mu$ ) gives information on a bond's or molecule's ionic character state (49). Ionic property is generally associated with molecules with a higher dipole moment value. Furthermore, dipole moments play a crucial role in forecasting a molecule's structure and reactivity. The dipole moments for the studied compounds; Lonchocarpol A, Broussonol E, Diplacol and Dexamethasone were 2.663, 4.122, 5.209, 5.334 respectively (Table 3). The computation of polarizability ( $\alpha_0$ ) and hyperpolarizability ( $\beta_0$  and  $\gamma_0$ ) in molecular systems is useful for describing charge delocalization and measuring NLO effects (51). More intriguingly, they've been used in pharmaceutical development. The coefficients in the Taylor series expansion depending on the energy in the external electric field (51, 52) are denoted as the first hyperpolarizability ( $\beta_0$ ) and associated properties ( $\mu$ ,  $\alpha_0$  and  $\gamma_0$ ) of the described compounds Lonchocarpol A, Broussonol E, Diplacol and Dexamethasone. The expansion can be expressed as follows for a weak homogenous external electric field:

$$E = E_0 - \sum \mu_i F^i - \frac{1}{2} \sum \alpha_{ij} F^i F^j - \frac{1}{6} \sum \beta_{ijk} F^i F^j F^k + \frac{1}{24} \sum \gamma_{ijkl} F^i F^j F^k F^l + \dots$$

11

Note,  $E_0$  describes the energy of the unperturbed molecules,  $F^i$  represents the field at the origin,  $\mu_i$ ,  $\alpha_{ij}$ ,  $\beta_{ijk}$  and  $\gamma_{ijkl}$  correlates to the dipole moment, static polarizability, first order hyperpolarizability and second order hyperpolarizability. The total dipole moment  $\mu$ , static mean polarizability  $\alpha_0$ , the mean first order hyperpolarizability  $\beta_0$  and second order hyperpolarizability  $\gamma_0$  can be estimated by the equations below;

$$\text{Dipole moment } \mu = \sqrt{\mu_x^2 + \mu_y^2 + \mu_z^2} \quad (12)$$

$$\text{Static mean polarizability } \alpha_0 = (\alpha_{xx} + \alpha_{yy} + \alpha_{zz}) / 3 \quad (13)$$

$$\text{Static first order hyperpolarizability } \beta = \sqrt{\beta_x^2 + \beta_y^2 + \beta_z^2} \quad (14)$$

$$\text{Where } \beta_x = 3/5 (\beta_{xxx} + \beta_{xyy} + \beta_{xzz}) \quad (15)$$

$$\beta_y = 3/5 (\beta_{yyy} + \beta_{yzz} + \beta_{yxx}) \quad (16)$$

$$\beta_z = 3/5 (\beta_{zzz} + \beta_{zxx} + \beta_{zyy}) \quad (17)$$

$$\beta_{\text{Total}} = \sqrt{(\beta_{xxx} + \beta_{xyy} + \beta_{xzz})^2 + (\beta_{yyy} + \beta_{yzz} + \beta_{yxx})^2 + (\beta_{zzz} + \beta_{zxx} + \beta_{zyy})^2} \quad (18)$$

$$\gamma = 1/5 [\gamma_{xxxx} \gamma_{yyyy} \gamma_{zzzz} + 2(\gamma_{xxx} + \gamma_{yyy} + \gamma_{zzz})] \quad (19)$$

Notably, any compounds with higher value of first order hyperpolarizabilities denotes an NLO active compound and vice versa. Table 4 shows that the hyperpolarizability value of Dexamethasone is  $(0.7207 \times 10^{-30})$  is 10 times higher than that of Lonchocarpol A  $(0.0586 \times 10^{-30})$ , Broussonol E  $(0.0017 \times 10^{-30})$  and Diplacol  $(0.0590 \times 10^{-30})$ . Collectively, this study proposed that Dexamethasone as the most suitable compound for NLO based technology.

Table 3  
The non-linear optics (NLO) measurements of the top four compounds.

Parameters	Lonchocarpol	Broussonol E	Diplacol	Dexamethasone
Dipole moment (Debye)				
$\mu_x$	-0.016	0.936	5.075	1.003
$\mu_y$	2.546	4.004	1.089	1.943
$\mu_z$	0.781	-0.284	0.444	4.865
$\mu$	2.663	4.122	5.209	5.334
Polarizability (a.u.)				
$\alpha_{xx}$	423.2262	422.1966	474.0150	276.5705
$\alpha_{xy}$	-32.1733	422.1966	20.7672	-1.9526
$\alpha_{yy}$	321.3188	415.5835	337.6663	249.1648
$\alpha_{xz}$	5.8622	5.8562	11.7997	-38.5436
$\alpha_{yz}$	12.2187	38.3700	32.3409	6.6118
$\alpha_{zz}$	252.3939	230.5271	228.9737	308.3070
$\alpha_0$	332.31294	356.10239	346.88497	278.01414
Hyperpolarizability (a.u.)				
$\beta_{xxx}$	-828.11534	-1758.35361	-857.13155	-105.90769
$\beta_{xxy}$	1274.91556	1770.96251	1087.95116	-11.22939
$\beta_{xyy}$	408.19522	-939.40438	392.33997	-56.47036
$\beta_{yyy}$	-205.66502	198.04721	-145.10306	-0.22422
$\beta_{xxz}$	218.15245	622.87825	-23.37222	-19.56624
$\beta_{xyz}$	-56.15189	19.08646	31.58709	14.60703
$\beta_{yyz}$	-40.72098	-90.27506	22.36855	30.11794
$\beta_{xzz}$	67.05907	86.15574	8.42037	164.77391
$\beta_{yzz}$	-12.20923	-74.49353	9.07706	-12.27861
$\beta_0$	678.2379	1946.6357	633.4487	83.4142
$\gamma_{xxxx}$	136082.88516	437948.46962	122946.68736	13932.57214
$\gamma_{yyyy}$	40946.55150	86024.86024	18258.69096	14983.28635
$\gamma_{zzzz}$	6622.48729	6562.67994	3978.16272	15251.43212
$\gamma_{xxyy}$	49373.55773	208421.66382	48042.22109	4810.78759
$\gamma_{xxzz}$	8548.39107	18233.01061	11992.55351	4799.66326
$\gamma_{yyzz}$	4755.42360	11210.83548	2029.91003	7556.43105
$\gamma_0$	61448.83940	205675.48909	53862.59096	15788.15525

Standard value for urea ( $\mu = 1.3732$  Debye,  $\beta_0 = 0.3728 \times 10^{-30}$  esu): **esu**-electrostatic unit. (For  $\alpha$ , 1 a.u is equal to  $0.1482 \times 10^{-24}$  esu. Similarly, for  $\beta$ , 1 a.u is equal to  $8.6393 \times 10^{-33}$  esu).

Table 4

The molecular electric dipole moment ( $\mu$ ), static polarizability ( $\alpha_0$ ), static first order hyperpolarizability ( $\beta_0$ ), static second order hyperpolarizability ( $\gamma_0$ ), of the top four compounds.

Compound	Dipole moment (Debye)	static polarizability ( $\alpha_0 \times 10^{-23}$ esu)	static first hyperpolarizability ( $\beta_0 \times 10^{-30}$ esu)	static second order hyperpolarizability ( $\gamma_0 \times 10^{-39}$ esu)
Lonchocarpol A	2.663	5.1226	0.0586	30949.9528
Broussonol E	4.122	5.2774	0.0017	103592.6267
Diplacol	5.209	5.1654	0.0590	32680.4170
Dexamethasone	5.334	4.1202	0.7207	7952.0242

### 3.5 Molecular docking and binding site analysis

#### 3.5.1 Inhibitory potential of promising phyto-drugs against SARS-CoV-2 Spike Glycoprotein, 3CLpro, PLpro and RdRp.

The 3CLpro also referred to as NSP5 mediates the maturation of Nsp5 which is vital in the lifecycle of the virus. The structural analysis and catalytic mechanism of 3CLpro using biophysical techniques have been widely investigated (53). Therefore, 3CLpro remained an important therapeutic target for the development of potential anti-coronavirus drug candidates. Peptide inhibitors and small-molecules are inhibitors targeting the SARS-CoV-2 3CL pro. From the molecular docking result, various molecular interactions including hydrogen bonding, hydrophobic, polar and pi-pi interactions were observed and analyzed while ranking the compounds based on their binding poses. Although, Nicotiflorin, Schaftoside, Acetoside and Mallophenol demonstrated an average binding energy of -11.20kcal/mol (Table 5). They were eliminated from further studies because of their undruggable properties. Interestingly, Lonchocarpol A, Broussonol E, Diplacol and Dexamethasone (reference compound) were selected for further analysis due to drug-like properties, molecular interactions and high binding energy.

Lonchocarpol A is a flavone which originate from *Lonchocarpus* and *Erythrina* species and have been reported for its biological activities including anti-cancer, insecticidal and antibacterial activity amongst others. Interestingly, Lonchocarpol A had also been synthesized using various synthetic methods have also received a great interest as compounds with numerous therapeutic benefits (54). Lonchocarpol A has a binding affinity of -8.644kcal/mol and hydrogen bond interactions with ARG188 based on his side hydroxyl group. All significant interaction exhibited by the compound were mainly due to its alkyl side group and phenyl ring. The alkyl groups present in the phenyl moiety interact with hydrophobic amino acids TYR54, PRO52, MET49, CYS44, VAL42, LEU27 and polar amino acids HIS41, ASN142, GLN189, THR190, GLN192, HIS164 (Fig. 3). The other notable interactions were pi-pi/charge interactions between the aromatic ring of Lochocarpol A with ASP48, ASP187, GLU166 and ARG188. The second selected molecule, diplacol showed shared similar hydrogen bond with amino acid ARG188 as in lonchocarpol A, however, the two dihydroxyphenyl and the alky group of the compounds were responsible for its hydrophobic and polar interactions (Fig. 3). Broussonol E have a binding energy of -8.069kcal/mol and also shows key biomolecular interactions within the 3CLpro active site. The reference compound (dexamethasone has the least binding energy). However, the top three compounds were proposed to have similar mechanism of action as dexamethasone since their share the same amino acid interactions with the targets.

Spike is the coronavirus's major structural protein, which assembles as a trimer into a unique corolla structure on the virus's surface. The spike protein mediates the virus interaction with the host cell by binding to the host Angiotensin-converting enzyme (ACE-2). Certain host cell proteases such as TMPRSS2 cleaves the spike protein into two subunit S1 and S2 which plays a key role in receptor recognition and the cell membrane fusion process (55). Therefore, blocking the coronavirus entry into the cell by targeting the spike glycoprotein have been greatly harnessed in the developments of therapeutic agents against coronavirus. From the virtual screening results, Rutin, Delphinidin 3-O-beta-D-sambubioside and hesperidin shows the highest binding energy of -10.941kcal/mol, -10.709kcal/mol and - 10.627kcal/mol respectively (Table 5). Unfortunately, these compounds failed the toxicity assessment and were eliminated from further study. Thus, only bioactive compounds such as diplacol, broussonol E and Luteolin were observed with promising drug-like properties and binding poses orientation. The protein-ligand contacts show the compounds established some essential hydrogen and hydrophobic interactions.

Papain-like proteinase (PLpro) plays a role in the cleavage of N-terminus of the replicase poly-protein to produce non-structural proteins including Nsp1, Nsp2 and Nsp3 which are involved in the virus replication (56). Thus, based on the key role played by PLpro in the virus replication and infection, it has received intense consideration as a therapeutic target for coronavirus inhibitors. There has been no FDA approved inhibitors of PLpro. Aucubin was recorded with the highest binding energy against PLpro with - 8.767kcal/mol. Aucubin high binding energy may be attributed to its structural basis including its imidazole ring. Nicotiflorin optimally occupied the binding pocket of the target (PLpro) which may be attributed to its ring system. The presence of multiple hydroxyl group at the Nicotiflorin structures establishes intermolecular hydrogen bonds.

Several other docked compounds including rutin, diplacol, hesperidin, kuromanin showed high binding energy against PLpro while establishing pi-pi and hydrophobic interactions with amino acid residues at the active site of PLpro (Table 6).

RNA-dependent RNA polymerase (RDRP: NSP 12) is a conserved protein in coronavirus with major function in coronavirus replication/transcription complex. Targeting NSp-12RdRp have been well documented for their little to no side effects on the host cell (57). However, there has been no specific RdRp inhibitor till present. Molecular docking results of RdRp following extra-precision approach shows the anti-viral potential of the docked compounds. Interestingly, Acetosides and cynarosides demonstrated the highest binding energy of -10.632kcal/mol and - 9.193kcal/mol respectively (Table 5).

Table 5  
Binding energy (Kcal/mol) of compounds against SARS-CoV-2 therapeutic targets

S/NS	Compounds	Spike glycoprotein RBD (6M0J)	Compounds	3CLPro (6M2N)	Compounds	PLPro (7CJM)	Compounds	RDRP (7D4F)
1	Rutin	-10.941	Nicotiflorin	-11.442	Aucubin	-8.767	Acteosides	-10.632
2	Delphinidin 3-O-beta-D-sambubioside	-10.709	Schaftoside	-11.389	Rutin	-8.698	Cynaroside	-9.193
3	Hesperidin	-10.627	Acteoside	-11.291	Nicotiflorin	-8.685	Hydroxycitric acid	-9.087
4	Acteoside	-10.033	Mallophenol B	-11.226	Mallophenol B	-8.106	Rutin	-8.704
5	Kuromanin	-9.902	Kolaflavanone	-10.496	Hesperidin	-7.671	Schaftoside	-8.347
6	Pelargonidin 3-glucoside	-9.684	Aucubin	-10.295	Cynaroside	-7.537	Bergenin	-8.127
7	Lauroside E	-9.599	Tanariflavanone C	-10.278	Kuromanin	-7.186	Kuromanin	-7.687
8	Nicotiflorin	-9.447	(+)-Gallocatechin gallate	-10.334	Schaftoside	-7.114	Mallophenol B	-7.680
9	diplacol	-8.733	Delphinidin 3-O-beta-D-sambubioside	-10.035	Pelargonidin 3-glucoside	-6.811	Lauroside E	-7.641
10	Myricetin	-8.725	Rutin	-8.987	Nymphaeol B	-6.687	Hydroxycitric acid	-7.629
11	Nymphaeol B	-8.291	Luteolin	-8.866	(+)-Gallocatechin gallate	-6.663	Pelargonidin 3-glucoside	-7.489
12	Schaftoside	-8.251	Nymphaeol C	-8.748	Macaranone A	-6.548	(+)-Gallocatechin gallate	-8.937
13	(+)-Gallocatechin gallate	-8.289	Macakurzin A	-8.723	Myricetin	-6.531	Delphinidin 3-O-beta-D-sambubioside	-7.333
14	Macakurzin A	-8.191	Isovitexin	-8.710	Bergenin	-6.378	Gallic acid	-7.122
15	Tanariflavanone D	-8.160	<b>Lonchocarpol A*</b>	<b>-8.644*</b>	Quercetin	-6.377	Catalpol	-7.017
16	Chlorogenic acid	-8.131	<b>Diplacol*</b>	<b>-8.576*</b>	Isovitexin	-6.277	Nicotiflorin	-6.819
17	Isovitexin	-8.096	Tomentosanol D	-8.470	Tanariflavanone C	-6.161	Aucubin	-6.752
18	Cynaroside	-7.991	Isolicoflavonol	-8.451	Lauroside E	-6.117	Tanariflavanone D	-6.739
19	Quercetin	-7.996	Fisetin	-8.459	Acteoside	-6.115	Hydroxycitric acid.1	-6.342
20	Bonnaniol	-7.904	Denticulaflavonol	-8.253	Nymphaeol A	-6.047	Macarangioside F	-6.255
21	Macakurzin A	-7.884	Glepidotin A	-8.231	diplacol	-5.972	Chlorogenic acid	-6.089
22	Aucubin	-7.818	Myricetin	-8.187	Catalpol	-5.733	Protocatehuic acid	-6.019
23	Broussonol E	-7.490	Catalpol	-8.164	Tomentosanol D	-5.692	Hesperidin	-5.997
24	Mallophenol B	-7.425	Macarangin	-8.134	Alnifoliol	-5.674	Cianidanol	-5.992
25	Luteolin	-7.414	Cynaroside	-8.066	Macakurzin A	-5.631	Tomentosanol D	-5.875

\*Selected compounds and their binding energy against 3CLpro for further molecular dynamics analysis.

S/NS	Compounds	Spike glycoprotein RBD (6M0J)	Compounds	3CLPro (6M2N)	Compounds	PLPro (7CJM)	Compounds	RDRP (7D4F)
26	Macarangin	-7.331	<b>Broussonol E*</b>	<b>-8.069*</b>	Isolicoflavonol	-5.602	Isovitexin	-5.871
27	Dexamethasone	-5.641	<b>Dexamethasone*</b>	<b>-5.302*</b>	Dexamethasone	-3.939	Dexamethasone	-2.946

\*Selected compounds and their binding energy against 3CLpro for further molecular dynamics analysis.

Table 6  
Molecular interaction profiling and docking score of top four compounds

Interacting Amino Acid Residues								
S/N	Lead Compounds against 3CLPro	Docking score (kcal/mol)	H-bond	Hydrophobic	Polar	Charged (Negative)	Charged (Positive)	Glycine
1	Lonchocarpol A	-8.644	ARG <sup>188</sup>	TYR54, PRO52, MET49, CYS44, VAL42, LEU27, CYS145, VAL186, ALA191, LEU167, PRO168, MET	HIS41, ASN142, GLN189, THR190, GLN192, HIS164	ASP48, ASP187, GLU166	ARG188	GLY143
2	diplacol	-8.576	ARG188	TYR54, PRO52, CYS44, MET49, MET165, CYS145, LEU27,	GLN189, HIS41, HIS164, ASN142, THR26, THR25, THR24	ASP48, GLU166, ASP187	ARG188	GLY143
3	Broussonol E	-8.069	ARG188	CYS145, CYS44, MET49, PRO52, TYR54, MET165, LEU167	THR26, THR25, THR24, HIS164, GLN192, THR190, GLN189, HIS41, ASN142	ASP48, ASP187, GLU166	ARG188	GLY143
4	Dexamethasone	-5.302	ARG188	PRO168, LEU167, MET165, MET49, CYS44, PRO52, TYR54	HIS164, GLN189, HIS41, ASN142	GLU166, ASP48, ASP187	ARG188	—

### 3.6 MM-GBSA binding energy of top inhibitors

Molecular mechanics generalized Born Surface Area (MM-GBSA) have been widely explored as an advanced computational approach to analyze binding energy with improved algorithm and solvation model. When compared to docking, post-scoring compounds using MM-GBSA has been demonstrated to have a better correlation to their reported binding affinity of docked complexes (58, 59). The MM-GBSA method is a more accurate way to estimate the free binding energies of protein-ligand complexes than docking scores. Post-docking MM/GBSA analysis of the docked complexes were -55.562kcal/mol, -49.137kcal/mol, -46.628kcal/mol and -39.605kcal/mol for Lonchocarpol A, Broussonol E, Diplacol and Dexamethasone respectively as shown in Fig. 4. The post-simulation MM/GBSA which further validate the binding affinity of the compounds shows similar binding energy with post-docking analysis.

### 3.7 Drug likeness and toxicity descriptors

Pharmacokinetic properties of the top 4 lead potential antiviral ligands were predicted, studied, and tabulated as shown in Table 4. It is clear that except (-)-Lonchocarpol A and Broussonol E, none penetrated the Blood-brain barrier. Under the adsorption and distribution, the Caco-2 permeability of the lead compounds show that Lonchocarpol A and Dexamethasone showed positive ions of Caco-2- permeability while Diplacol and Broussonol E showed negative ion of Caco-2- permeability.

The action of the four lead compounds on the P-glycoprotein (substrate) showed that Lonchocarpol A, Diplacol and Broussonol E are non-substrate, while only Dexamethasone showed the level of substrate to the glycoprotein (Table 7). Lonchocarpol A, Diplacol and Broussonol E are good inhibitor to the glycoprotein from COVID-19 while only Dexamethasone show its non-inhibiting property. About the LogS (aqueous solubility), the Broussonol E have the least solubility with -3.567, followed by Dexamethasone with -3.703 which is greater than Broussonol E, Lonchocarpol A have solubility value in the aqueous of -3.925 and the highest solubility value out of the four lead compounds in the aqueous state is Diplacol with value of -4.285. All the compounds complexes exhibit non-inhibitor on Renal organic cation transporter 2 (OCT2) except Dexamethasone which show inhibiting property.

For the metabolism, the CYP450 2C9 (substrate) and CYP450 2D6 (substrate) showed that all the four lead compounds are non-substrate in nature, and CYP450 2D6 (inhibition) showed the lead compounds as Non-Inhibitor. For CYP450 2C9 (inhibition), CYP450 1A2, and CYP450 2C19 showed that three of the lead compounds are inhibitor in nature while only the Dexamethasone was Non-Inhibitor in nature.

For the Ames toxicity, all the three compounds are Non-Toxic only the Diplacol is toxic in nature. In the analysis of hERG inhibition and Carcinogenicity, all the four lead compounds exhibit inhibiting properties and Non-carcinogenic ability. The Rat LD50 is higher on Lonchocarpol A with value point of 2.705 and lower on Broussonol with value of 2.129. Thus, natural phytochemicals are not naturally occurring and reported negligible toxicity when tested in-vitro, hence could be a promising drug candidate and can be tested in-vitro then in-vivo. Lethal doses (LD50) of all the natural compounds were higher when compared to chemical drugs, which denotes that even at a higher dosage, natural compounds are less toxic compared to chemically synthesized drugs (60). Thus, chemical drugs are toxic from the pharmacokinetic predictions compared to natural compounds, moreover, natural compounds have shown potential against several diseases with the least side effects. The drug-likeness properties (Table 7) of the compounds shows they are druggable compounds with no violations of the Lipinski's assessment and Verber's rules (Table 8).

Table 7  
Pharmacokinetics profile of top four compounds

Models	Lonchocarpol A	Diplacol	Broussonol E	Dexamethasone
<b>Absorption and Distribution</b>				
Blood brain barrier	BBB-	BBB+	BBB-	BBB+
Caco-2 permeability	Caco-2 <sup>+</sup>	Caco-2 <sup>-</sup>	Caco-2 <sup>-</sup>	Caco-2 <sup>+</sup>
P-glycoprotein (substrate)	Non-substrate	Non-substrate	Non-substrate	Substrate
P-glycoprotein (inhibitor)	Inhibitor	Inhibitor	Inhibitor	Non-inhibitor
LogS (aqueous solubility)	-3.925	-4.285	-3.567	-3.703
Renal organic cation transporter 2 (OCT2)	Non-inhibitor	Non-inhibitor	Non-inhibitor	Inhibitor
<b>Metabolism</b>				
CYP450 2C9 (substrate)	Non-substrate	Non-substrate	Non-substrate	Non-substrate
CYP450 2C9 (inhibition)	Inhibitor	Inhibitor	Inhibitor	Non-inhibitor
CYP450 2D6 (substrate)	Non-substrate	Non-substrate	Non-substrate	Non-substrate
CYP450 2D6 (inhibition)	Non-inhibitor	Non-inhibitor	Non-inhibitor	Non-inhibitor
CYP450 3A4 (substrate)	Substrate	Non-substrate	Non-substrate	Substrate
CYP450 3A4 (inhibition)	Non-inhibitor	Inhibitor	Inhibitor	Non-inhibitor
CYP450 1A2	Inhibitor	Inhibitor	Inhibitor	Non-inhibitor
CYP450 2C19	Inhibitor	Inhibitor	Inhibitor	Non-inhibitor
<b>Toxicity</b>				
Ames toxicity	Non-toxic	Toxic	Non-toxic	Non-toxic
hERG inhibition	Inhibitor	Inhibitor	Inhibitor	Inhibitor
Carcinogenicity	Non-carcinogenic	Non-carcinogenic	Non-carcinogenic	Non-carcinogenic
Acute oral toxicity	III	III	III	III
Rat LD50	2.705	2.591	2.129	2.189ss

Table 8  
Drug-likeness prediction of top four compounds

COMPOUNDS	MW	HBA	HBD	VEBER RULE	ROF
Lonchocarpol A	408.49 g/mol	5	3	TPSA = 86.99 Å <sup>2</sup> Num. rotatable bonds = 5	0
Diplacol	440.49 g/mol	7	5	TPSA = 127.45 Å <sup>2</sup> Num. rotatable bonds = 6	0
Broussonol E	438.47 g/mol	7	5	TPSA = 131.36 Å <sup>2</sup> Num. rotatable bonds = 5	0
Dexamethasone	392.46 g/mol	6	3	TPSA = 94.83 Å <sup>2</sup> Num. rotatable bonds = 2	0
MW; Molecular weight, HBA; Hydrogen bond acceptor, HBD; Hydrogen bond donor; TPSA; Topological Surface Area, ROF; Rule of five.					

### 3.8 Molecular Dynamics Simulation of the complexes

Molecular dynamics (MD) simulation is an essential tool that help in the study of macromolecules like nucleosomes, ribosomes, membrane proteins, organic solids, proteins-ligand complexes, etc. and has evolved rapidly over the last 4 decades due to advances in force fields, thanks to the development of quantum physics and computational chemistry (61). The simulation is widely used in the analysis of the structure to function relationship of protein and protein-ligand complexes. The current generation molecular dynamics mimic the actual biological systems with a potential of simulation up to 100ns for each complexes and their behavior in the order of nanoseconds with appropriate system configurations using high-speed supercomputers. It takes thousand to several million steps and involves intra and interatomic interactions simulated simultaneously for which supercomputers play a vital role in attaining so. It is very essential to study the simulation in the order of shortest duration preferably femtoseconds since the structural and functional properties of biomolecules concerning to nano and microseconds (62).

After the chemical profiling, the association of compound complexes were examined and the dynamic stability of screened compounds was studied using MD simulation at 100 ns in terms of root mean square deviation, root mean square fluctuations and molecular contacts (Figure below). This was achieved with the aid of Desmond module integrated in the Schrodinger suite. Analyzing through the molecular dynamics simulation at the atomistic level, all the compounds was found to be relatively stable through the MD simulation period (Fig. 5). Lonchocarpol A-3CLpro complexes was found to be stable within 0-50ns. However, fluctuations were observed from 55ns to 65ns before the ligand retain its stability (Fig. 5). RMSF analysis explicitly shows that some amino acid residues (PHE-3, ARG-4, GLY-138 and GLU-255) contributed towards the ligand fluctuations (Fig. 6). Clearly, Broussonol E was found to be stable when complex with the protein backbone with subtle fluctuation recorded at 25-35ns and 65-75ns. RMSF analysis of Broussonol E shows its residue index and also established molecular contacts largely dominated by water bridges and hydrophobic interactions (Fig. 6). Diplacol demonstrated varying degree of fluctuations between 0-20ns. Interestingly, it was found to be very stable from 25ns-100ns. Although, a slight increase in RMSD value of the ligand was observed toward the end (90-100ns) of the simulation period as shown in the trajectory. The reference compound (dexamethasone) reached a peak of RMSD 2.0Å at 20ns and also established essential interaction profiling such as hydrogen and water bridges. Our results herein suggest that the binding of the compounds may prompt conformational alterations as shown in the figure below. In consistent with this, the analysis of MMGBSA with trajectory against MMBGSA without trajectory residue number showed that the compound complexes showed higher oscillations in backbone residues when compared to other complexes in the systems as shown in the figure below. This is consistent with the docking results of the four lead compounds that showed the highest binding free energy to other compounds with low or least binding free energy of -7.3 and -8.1 kcal/mol as shown in the table below.

The establishment and immovability of H-bonds were inspected over the simulation period (Fig. 7). H-bond features are essential factor in drug design and discovery due to their irreplaceable role in drug specificity, metabolism and absorption (63). From Fig. 7 below, the results illustrated that the four lead compounds could establish at least one hydrogen bond with amino acid residues. Thus, the stability of complexes was maintained by H-bonds formation with active site residues. According to the docking and MD simulation analyses, the four lead compounds showed good affinity towards COVID-19 in comparison to the other compounds.

However, Lonchocarpol A showed a high docking score (-8.644 kcal/mol) and was able to form pi-stacking interactions the essential amino acids of COVID-19 binding domain. The MD simulation of the complexes in the study was very helpful in analyzing the conformational stability and dynamics of the protein and protein-ligand complexes at different nanosecond time intervals, fluctuations, and their deviations from the reference structure on COVID-19.

## Conclusion

Finally, sequencing, docking, molecular dynamics simulation, and MM-GBSA studies of chemical libraries against by the RBD of the protein target yielded a strong associative target molecule that can bind to the RBD domain at the RBD-ACE2 interface and thus inhibit the ACE2 interaction to the COVID-19 spike protein. As a result, we propose that the hit compound or target be used as a lead molecule in the development of new chemical libraries as inhibitors of the SARS-CoV-2 spike protein in order to prevent host cell contact.

## Declarations

Authors have no conflict of interest regarding this article.

## Funding

This study received no external funding

## Author contributions

T.A.B conceptualized and design the study. T.A.B., O.S.C., and A.T.A., wrote the original draft of the article. U.C.O., I.O.J., and O.A.S., performed compounds library curation, and high-throughput virtual screening. T.A.B, E.A.O, O.M.I., and I.O.O. performed molecular docking and pharmacokinetics study. T.A.B., O.S.C., A.D.A. and T.A.S. performed molecular dynamics simulation and post-simulation analysis. T.A.B and P.O.C. performed quantum chemical calculation. U.C.O, I.O.J., A.D.A., and E.A.O assisted with data collection and editing. D.A.O and G.E.B supervised the project. All authors read and approved the final manuscript.

## Availability of Data and Materials

The dataset analyzed during the current study are available in the Protein Data Bank repository.

Spike glycoprotein RBD (6M0J): <https://www.rcsb.org/structure/6M0J>

3CLPro (6M2N): <https://www.rcsb.org/structure/6M2N>

PLPro (7CJM): <https://www.rcsb.org/structure/7CJM>

RDRP (7D4F): <https://www.rcsb.org/structure/7D4F>

## References

1. Chan, J. F.-W., Yuan, S., Kok, K.-H., To, K. K.-W., Chu, H., Yang, J., Xing, F., Liu, J., Yip, C. C.-Y., Poon, R. W.-S., et al. A Familial Cluster of Pneumonia Associated with the 2019 Novel Coronavirus Indicating Person-to-Person Transmission: A Study of a Family Cluster. *Lancet* 2020, 395 (10223), 514–523.
2. Luk HKH, Li X, Fung J, Lau SKP, Woo PCY. Molecular epidemiology, evolution and phylogeny of SARS coronavirus. *Infect Genet Evol* 2019,71:21–30. <https://doi.org/10.1016/j.meegid.2019.03.001>.
3. Xu C, Ke Z, Liu C, Wang Z, Liu D, Zhang L, et al. Systemic in silico screening in drug discovery for Coronavirus Disease (COVID-19) with an online interactive web server, *J Chem Inf Model*. <http://doi.org/10.1021/acs.jcim.0c00821>.
4. Adedeji, A. O., Singh, K., Calcaterra, N. E., DeDiego, M. L., Enjuanes, L., Weiss, S., Sarafianos, S. G. Severe Acute Respiratory Syndrome Coronavirus Replication Inhibitor That Interferes with the Nucleic Acid Unwinding of the Viral Helicase. *Antimicrob. Agents Chemother.* 2012, 56 (9), 4718–4728. <https://doi.org/10.1128/AAC.00957-12s>
5. Yu, M.-S., Lee, J., Lee, J. M., Kim, Y., Chin, Y.-W., Jee, J.-G., Keum, Y.-S., Jeong, Y.-J. Identification of Myricetin and Scutellarein as Novel Chemical Inhibitors of the SARS Coronavirus Helicase, NsP13. *Bioorg. Med. Chem. Lett.* 2012, 22 (12), 4049–4054. <https://doi.org/10.1016/j.bmcl.2012.04.081>
6. Jia, Z., Yan, L., Ren, Z., Wu, L., Wang, J., Guo, J., Zheng, L., Ming, Z., Zhang, L., Lou, Z., Rao, Z. Delicate Structural Coordination of the Severe Acute Respiratory Syndrome Coronavirus Nsp13 upon ATP Hydrolysis. *Nucleic Acids Res.* 2019, 47 (12), 6538–6550. <https://doi.org/10.1093/nar/gkz409>.

7. Seah, I. and Agrawal, R. (2020) Can the coronavirus disease 2019 (COVID-19) affect the eyes? A review of coronaviruses and ocular implications in humans and animals. *Ocul. Immunol. Inflamm.* 28, 391–395
8. Liu, C. et al. (2020) Research and development on therapeutic agents and vaccines for COVID-19 and related human coronavirus diseases. *ACS Cent. Sci.* 6, 315–331
9. Chen Y, Liu Q, Guo D. Emerging coronaviruses: genome structure, replication, and pathogenesis. *J Med Virol* 2020,92:418e23.
10. Omrani AS, Saad MM, Baig K, Bahloul A, Abdul-Matin M, Alaidaroos AY, et al. Ribavirin and interferon alfa-2a for severe Middle East respiratory syndrome coronavirus infection: a retrospective cohort study. *Lancet Infect Dis* 2014,14:1090e5
11. Ge XY, Li JL, Yang XL, Chmura AA, Zhu G, Epstein JH, et al. Isolation and characterization of a bat SARS-like coronavirus that uses the ACE2 receptor. *Nature* 2013,503:535e8.
12. Han DP, Penn-Nicholson A, Cho MW. Identification of critical determinants on ACE2 for SARS-CoV entry and development of a potent entry inhibitor. *Virology* 2006,350:15e25
13. Li W, Moore MJ, Vasilieva N, Sui J, Wong SK, Berne MA, et al. Angiotensin-converting enzyme 2 is a functional receptor for the SARS coronavirus. *Nature* 2003,426:450e4
14. Zumla A, Chan JF, Azhar EI, Hui DS, Yuen KY. Coronaviruses: drug discovery and therapeutic options. *Nat Rev Drug Discov* 2016,15: 327e47.
15. Chan JF, Chan KH, Kao RY, To KK, Zheng BJ, Li CPY, et al. Broad-spectrum antivirals for the emerging Middle East respiratory syndrome coronavirus. *J Infect* 2013,67:606e16
16. de Wilde AH, Jochmans D, Posthuma CC, Zevenhoven-Dobbe JC, van Nieuwkoop S, Bestebroer TM, et al. Screening of an FDA-approved compound library identifies four small-molecule inhibitors of Middle East Respiratory syndrome coronavirus replication in cell culture. *Antimicrob Agents Chemother* 2014,14:4875e84.
17. Dyal J, Coleman CM, Hart BJ, Venkataraman T, Holbrook MR, Kindrachuk J, et al. Repurposing of clinically developed drugs for treatment of Middle East respiratory syndrome coronavirus infection. *Antimicrob Agents Chemother* 2014,58:4885e93.
18. Omrani AS, Saad MM, Baig K, Bahloul A, Abdul-Matin M, Alaidaroos AY, et al. Ribavirin and interferon alfa-2a for severe Middle East respiratory syndrome coronavirus infection: a retrospective cohort study. *Lancet Infect Dis* 2014,14:1090e5
19. Ling, C. (2020). Traditional Chinese medicine is a resource for drug discovery against 2019 novel coronavirus (SARS-CoV-2). *J. Integr. Med.* 18 (2), 87–88. doi:10.1016/j.joim.2020.02.00
20. World Health Organization (2004). SARS: clinical trials on treatment using a combination of traditional Chinese medicine and Western medicine. Beijing: World Health Organization.
21. Dudani, T., and Saraogi, A. (2020). Use of herbal medicines on coronavirus. *Acta Sci. Pharm. Sci.* 11 (6), 416–419. doi:10.31080/asps.2020.04.0518
22. Vellingiri, B., Jayaramayya, K., Iyer, M., Narayanasamy, A., Govindasamy, V., Giridharan, B., et al. (2020). COVID-19: a promising cure for the global panic. *Sci. Total Environ.* 725, 138277. doi:10.1016/j.scitotenv.2020.138277
23. Kim, H. Y., Eo, E. Y., Park, H., Kim, Y. C., Park, S., Shin, H. J., et al. (2010). Medicinal herbal extracts of *Sophorae radix*, *Acanthopanax cortex*, *Sanguisorbae radix* and *Torilis fructus* inhibit coronavirus replication in vitro. *Antivir. Ther.* 15 (5), 697–709. doi:10.3851/IMP1615
24. Wu, C. Y., Jan, J. T., Ma, S. H., Kuo, C. J., Juan, H. F., Cheng, Y. S. E., et al. (2004). Small molecules targeting severe acute respiratory syndrome human coronavirus. *Proc. Natl. Acad. Sci. USA* 101 (27), 10012–10017. doi:10.1073/pnas.0403596101
25. Wang, S. Q., Du, Q. S., Zhao, K., Li, A. X., Wei, D. Q., and Chou, K. C. (2007). Virtual screening for finding natural inhibitor against cathepsin-L for SARS therapy. *Amino Acids* 33 (1), 129–135. doi:10.1007/s00726-006-0403-1
26. Stewart JJP (1990) MOPAC: a semiempirical molecular orbital program. *J Comput Aided Mol Des* 4:1–103 . <https://doi.org/10.1007/BF00128336>
27. Dutra JDL, Filho MAM, Rocha GB, Freire RO, Simas AM, Stewart JJP (2013) Sparkle/PM7 lanthanide parameters for the modelling of complexes and materials. *J Chem Theory Comput* 9:3333–3341 . <https://doi.org/10.1021/ct301012h>
28. Klamt A, Schuurmann G (1993) COSMO: A new approach to dielectric screening in solvents with explicit expressions for the screening energy and its gradient. *J Chem Soc Perkin Trans 2*:799–805 . <https://doi.org/10.1039/P29930000799>
29. Hanwell MD, Curtis DE, Lonie DC, Vandermeersch T, Zurek E, Hutchison GR (2012) Avogadro: An advance semantic chemical editor, visualization, and analysis platform. *J Cheminform* 4:17 . <https://doi.org/10.1186/1758-2946-4-17>
30. Chukwuemeka PO, Umar HI, Iwaloye O, Oretade OM, Olowosoke CB, Oretade OJ, Elabiyi MO (2021) Predictive hybrid paradigm for cytotoxic activity of 1,3,4-thiadiazole derivatives as CDK6 inhibitors against human (MCF-7) breast cancer cell line and its structural modifications: rational for novel cancer therapeutics. *J Biomol Struct Dyn.* <https://doi.org/10.1080/07391102.2021.1913231>
31. Hanson RM (2010) Jmol - a paradigm shift in crystallographic visualization. *J Appl Crystallogr* 43:1250–1260 . <https://doi.org/10.1107/S0021889810030256>

32. Sastry GM, Adzhigirey M, Day T, Annabhimoju R, Sherman W. Protein and ligand preparation: parameters, protocols, and influence on virtual screening enrichments. *J Comput Aided Mol Des.* 2013, 27: 221–34.
33. Balogun TA, Ipinloju N, Abdullateef OT, et al. Computational Evaluation of Bioactive Compounds from *Colocasia affinis* Schott as a Novel EGFR Inhibitor for Cancer Treatment. *Cancer Inform.* 2021,20:11769351211049244. doi:10.1177/11769351211049244
34. Friesner RA, Banks JL, Murphy RB, et al. Glide: A new approach for rapid, accurate docking and scoring. 1. Method and assessment of docking accuracy. *J Med Chem.* 2004,47:1739-1749
35. Schrödinger Release 201 8-4: Maestro Schrödinger. New York, NY: LLC, 2018
36. Parrinello M, Rahman A (1981) Polymorphic transitions in single crystals: A new molecular dynamics method. *J Appl Phys* 52:7182–7190
37. Darden T, York D, Pedersen L (1993) Particle mesh Ewald: an N-log (N) method for Ewald sums in large systems. *J Chem Phys* 98:10089–10092
38. Balogun TA, Iqbal MN, Saibu OA, et al. Discovery of potential HER2 inhibitors from *Mangifera indica* for the treatment of HER2-Positive breast cancer: an integrated computational approach *J Biomol Struct Dyn.* 2021,1-13.
39. (39)Schrödinger Release 2020–2: Prime, Schrödinger. New York, NY: LLC, 2020.
40. Genheden S, Ryde U. The MM/PBSA and MM/GBSA methods to estimate ligand-binding affinities. *Expert Opin Drug Discov.* 2015,10:449-461
41. Cheng F, Li W, Zhou Y, et al. ADMET-SAR: a comprehensive source and free tool for assessment of chemical ADMET properties. *J Chem Inf Model.* 2012,52:e3105.
42. Daina A, Michielin O, Zoete V (2017) SwissADME: A free web tool to evaluate pharmacokinetics, drug-likeness and medicinal chemistry friendliness of small molecules. *Sci Rep* 7:42717 . <https://doi.org/10.1038/srep42717>
43. Lipinski CA, Lombardo F, Dominy BW, Feeney PJ. Experimental and computational approaches to estimate solubility and permeability in drug discovery and development settings. *Adv Drug Deliv Rev.* 2001,46:3-26
44. Pearson RG (1986) Absolute electronegativity and hardness correlated with molecular orbital theory. *Proc Natl Acad Sci USA* 83:8440–8441 . <https://doi.org/10.1073/pnas.83.22.8440>
45. Sylaja B, Gunasekaran S, Srinivasan S (2017) Vibrational, NLO, NBO, NMR, frontier molecular orbital and molecular docking studies of diazepam. *Mater Res Innov.*<https://doi.org/10.1080/14328917.2017.1324356>
46. Phillips JC (1961) Generalized Koopmans' Theorem. *Phys Rev* 123:420 . <https://doi.org/10.1103/PhysRev.123.420>
47. V. Arjunan, S. Mohan, Fourier transform infrared and FT-Raman spectra, assignment, ab initio, DFT and normal co-ordinate analysis of 2-chloro-4-methyl-aniline and 2-chloro-6-methylaniline, *Spectrochim. Acta Part A Mol Biomol Spectrosc* 72 (2) (2009) 436–444
48. R.G. Pearson, Hard and soft acids and bases-the evolution of a chemical concept, *Coord. Chem. Rev.* (1990) 403–425
49. Sylaja B, Gunasekaran S, Srinivasan S (2017) Vibrational, NLO, NBO, NMR, frontier molecular orbital and molecular docking studies of diazepam. *Mater Res Innov.* <https://doi.org/10.1080/14328917.2017.1324356>
50. (50)Muhammad S, Lai C-H, Al-Sehemi AG, Alshahrani T, Iqbal J, Ayub K (2021) Exploring the twisted molecular configurations for tuning their optical and nonlinear optical response properties: A quantum chemical approach. *J Mol Graph Model* 102:107766 .<https://doi.org/10.1016/j.jmgm.2020.107766>
51. (51)Maragatham G, Selvarani S, Rajakumar P, Lakshmi S (2019) Structure determination and quantum chemical analysis of chalcone derivatives. *J Mol Struct* 1179:568–575 .<https://doi.org/10.1016/j.molstruc.2018.11.048>
52. (52)Muthu S, Ramachandran G, Paulraj RI, Swaminathan T (2014) Quantum mechanical study of the structure and spectroscopic (FTIR, FT-Raman), first-order hyperpolarizability and NBO analysis of 1, 2-benzoxazol-3-ylmethane sulfonamide. *Spectrochim Acta Part A Mol Biomol Spectrosc* 128:603–613 .<https://doi.org/10.1016/j.saa.2014.02.183>
53. (53)Pillaiyar T, Manickam M, Namasivayam V, Hayashi Y, Jung SH. An overview of severe acute respiratory syndrome-coronavirus (SARSCoV) 3CL protease inhibitors: peptidomimetics and small molecule chemotherapy. *J Med Chem* 2016,59:6595e628.
54. (54)Salvatore MJ, King AB, Graham AC, Onishi HR, Bartizal KF, Abruzzo GK, Gill CJ, Ramjit HG, Pitzenberger SM, Witherup KM. Antibacterial activity of Ionchocarpol A. *J Nat Prod.* 1998 May,61(5):640-2. doi: 10.1021/np9703961.
55. Millet JK, Whittaker GR. Host cell proteases: critical determinants of coronavirus tropism and pathogenesis. *Virus Res* 2015,202:120e34.
56. Li SW, Wang CY, Jou YJ, Huang SH, Hsiao LH, Wan L, et al. SARS coronavirus papain-like protease inhibits the TLR7 signaling pathway through removing Lys63-linked polyubiquitination of TRAF3 and TRAF6. *Int J Mol Sci* 2016,17:678.
57. (57)Ruan, Z., Liu, C., Guo, Y., He, Z., Huang, X., Jia, X., Yang, T. SARS-CoV-2 and SARS-CoV: Virtual Screening of Potential Inhibitors Targeting RNA-Dependent RNA Polymerase Activity (NSP12). *J. Med. Virol.* 2020, DOI: 10.1002/jmv.26222.
58. (58)Tripathi, S.K., Muttineni, R., Singh, S.K. Extra precision docking, free energy calculation and molecular dynamics simulation studies of CDK2 inhibitors. *Journal of theoretical biology* 2013, 334, 87-100,<https://doi.org/10.1016/j.jtbi.2013.05.014>

59. (59)Greenidge, P. A., Kramer, C., Mozziconacci, J. C., & Wolf, R. M. (2013). MM/GBSA binding energy prediction on the PDBbind data set: Successes, failures, and directions for further improvement. *Journal of Chemical Information and Modeling*, 53(1), 201–209. <https://doi.org/10.1021/ci300425v>
60. (60)Benfenati, E., Benigni, R., Demarini, D. M., Helma, C., Kirkland, D., Martin, T. M., Mazzatorta, P., Ou edraogo-Arras, G., Richard, A. M., Schilter, B., Schoonen, W. G. E. J., Snyder, R. D., & Yang, C. (2009). Predictive models for carcinogenicity and mutagenicity: Frameworks, state-of-the-art, and perspectives. *Journal of Environmental Science and Health. Part C, Environmental Carcinogenesis & Ecotoxicology Reviews*, 27(2), 57–90.
61. (61)Mekni, N., De Rosa, M., Cipollina, C., Gulotta, M. R., De Simone, G., Lombino, J., Padova, A., & Perricone, U. (2019). In silico insights towards the identification of NLRP3 druggable hot spots. *International Journal of Molecular Sciences*, 20(20), 4974. <https://doi.org/10.3390/ijms20204974>
62. (62)Liang, Z., Liu, F., Grundke-Iqbal, I., Iqbal, K., & Gong, C.-X. (2007). Downregulation of cAMP-dependent protein kinase by over-activated calpain in Alzheimer disease brain. *Journal of Neurochemistry*, 103(6), 2462–2470. <https://doi.org/10.1111/j.1471-4159.2007.04942.x>
63. (63)Kurczab, R. (2017). The evaluation of QM/MM-driven molecular docking combined with MM/GBSA calculations as a halogen-bond scoring strategy. *Acta Crystallographica Section B, Structural Science, Crystal Engineering and Materials*, 73(Pt 2), 188–194. <https://doi.org/10.1107/S205252061700138X>

## Figures

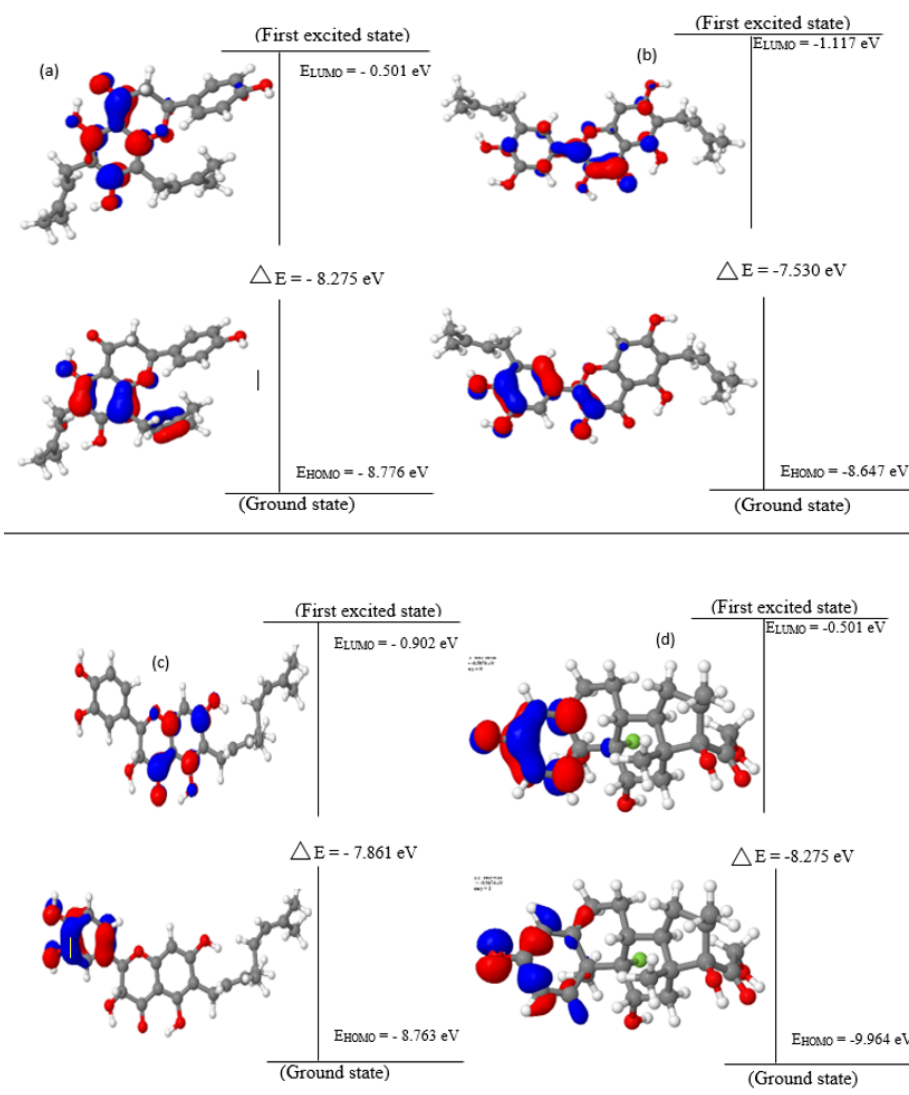
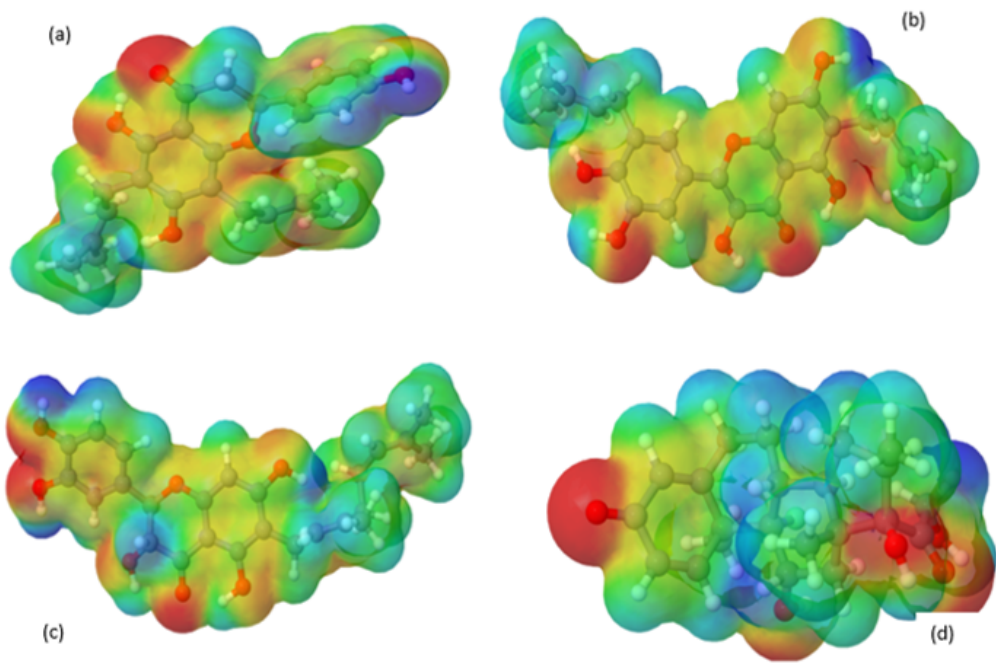


Figure 1

HOMO, LUMO and Band Gap Energy ( $\Delta E$ ) of the top four compounds (a) Lonchocarpol A (b) Broussonol E (c) Diplacol (d) Dexamethasone



**Figure 2**

Molecular electron potential (MEP) of the top four compounds (a) Lonchocarpol A (b) Broussonol E (c) Diplacol (d) Dexamethasone



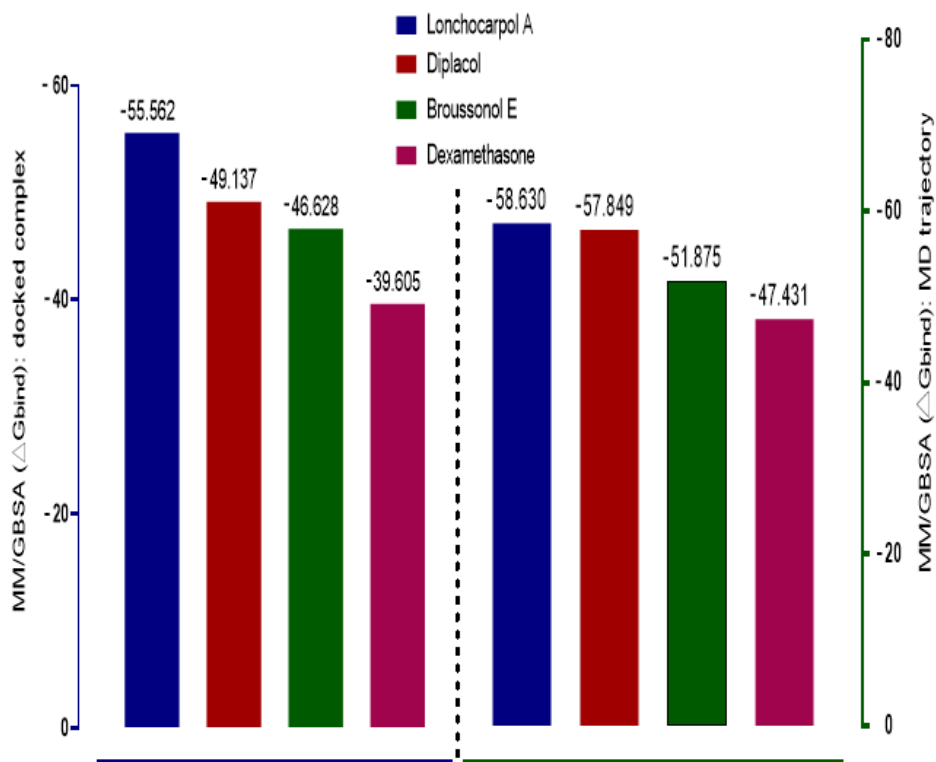


Figure 4

Graphical Representation of Prime/MM-GBSA binding energy ( $\Delta G_{bind}$ ) for docked complex and MD trajectory. The left frame (blue) denotes the post-docking MM-GBSA binding energy while the right frame (green) signifies the MM-GBSA binding energy of post-simulation analysis.

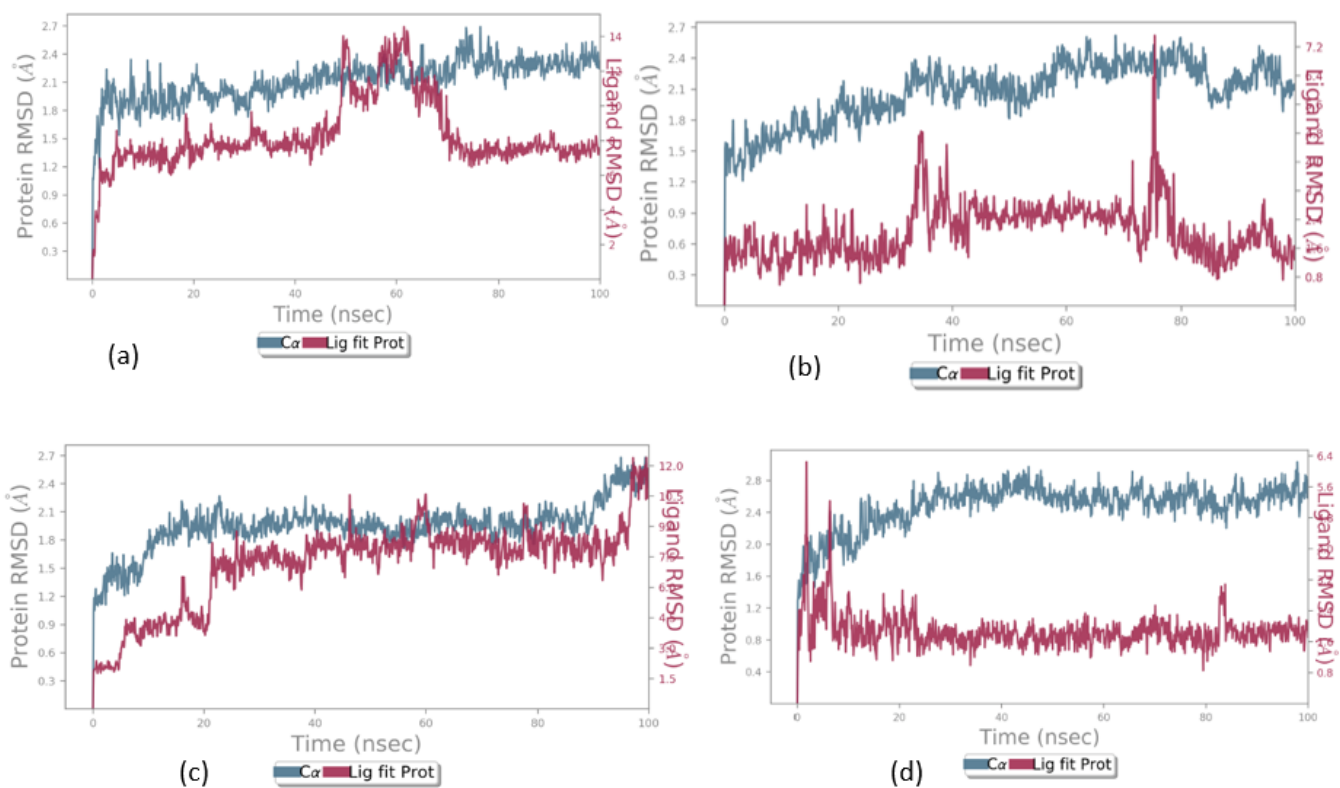
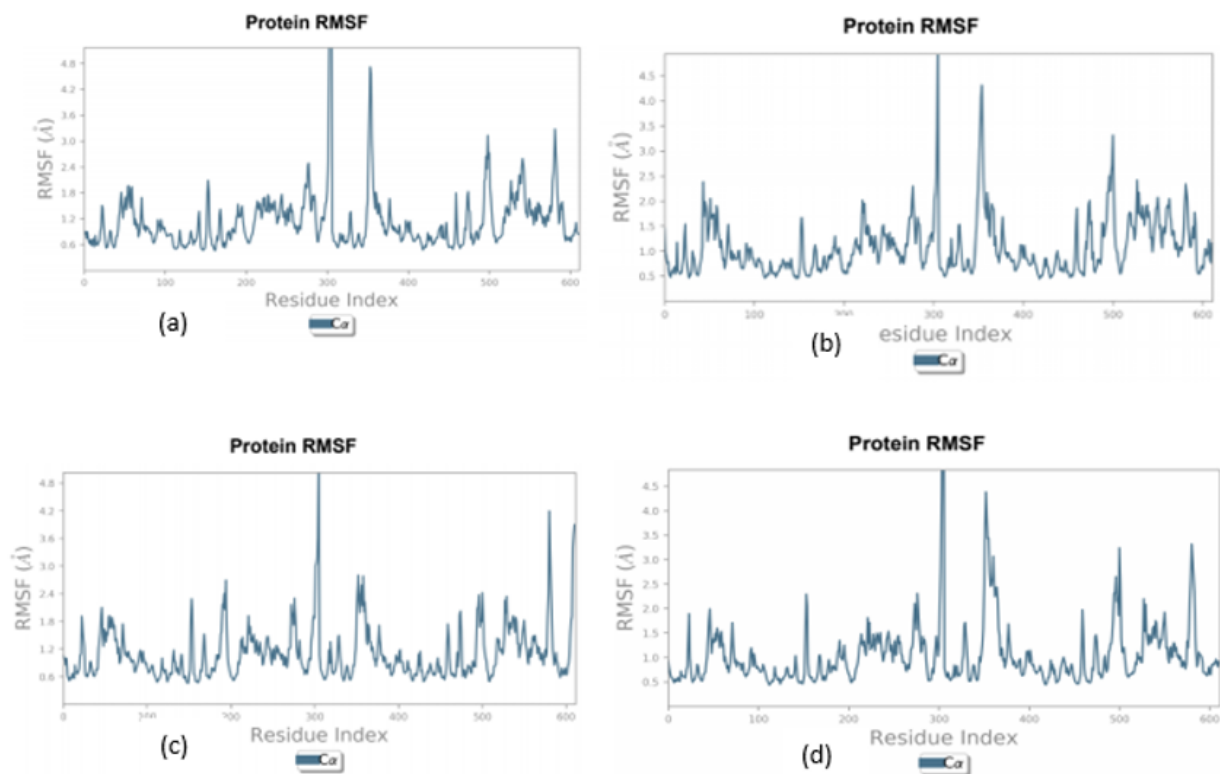


Figure 5

Calculated RMSD values for alpha carbon (C $\alpha$ ) atoms (blue curve) of 3CL Protease and protein fit ligands viz, (a) Lochocarpol A (b) Broussonol E (c) Diplacol (d) Dexamethasone were plotted with respect to 100ns simulation period



**Figure 6**

Line representation of the evolution of Root Mean Square Fluctuation of 3CL Protease C $\alpha$  during the 100ns MD simulation (a) Lonchocarpol A (b) Broussonol E (c) Diplacol (d) Dexamethasone

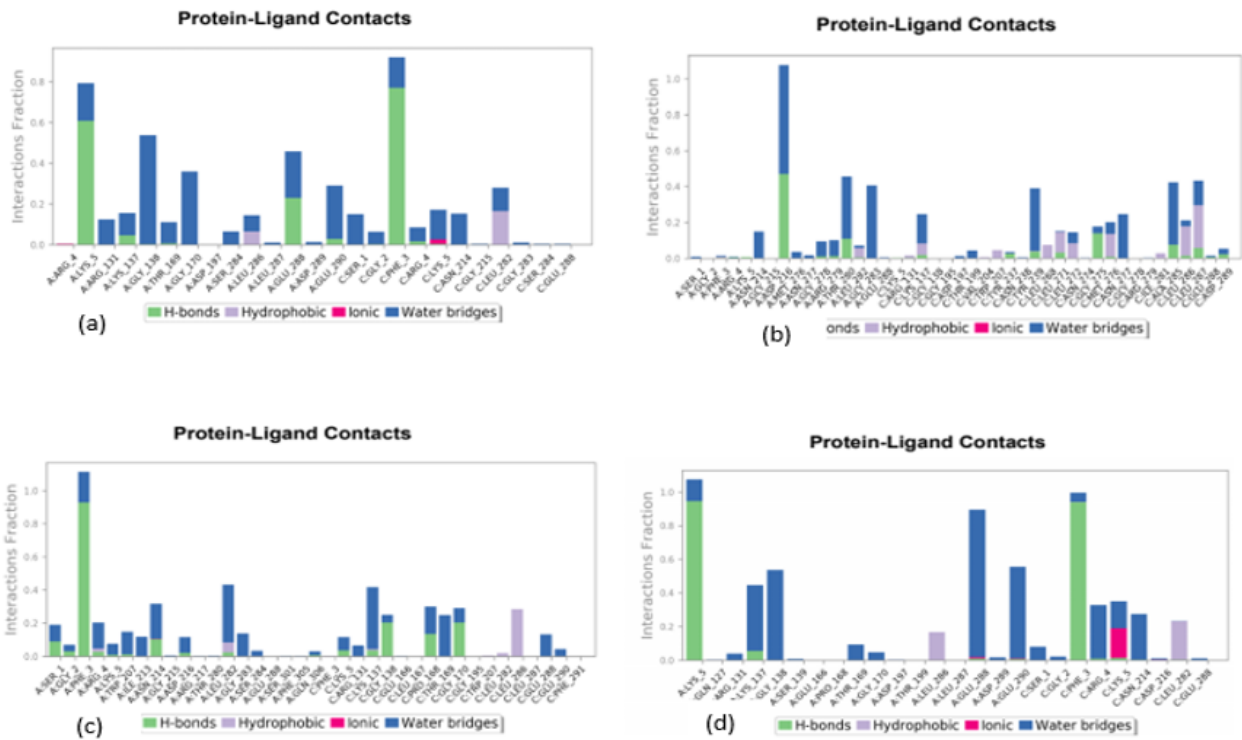


**Figure 7**

Post simulation analysis of protein-ligand interaction mapping (a) Lonchocarpol A - 3CL Pro complex (b) Broussonol E -3CL Pro complex (c) Diplacol - 3CL Pro (d) Dexamethasone - 3CL Pro